Modeling Hall Thruster Plume Expansion in Vacuum Chamber and Space Environments

IEPC-2025-216

Presented at the 39th International Electric Propulsion Conference, Imperial College London, London,
United Kingdom
14-19 September 2025

Charles P. Lipscomb, Iain D. Boyd, University of Colorado Boulder, Boulder, CO, USA 80303

Declan G. Brick[‡], and Benjamin A. Jorns[§] University of Michigan, Ann Arbor, MI, USA 48109

Hall-effect thrusters tested in ground-based vacuum chambers are subject to facility effects, which complicate the reliable extrapolation of experimental results to space environments. To obtain reliable predictions of in-space performance and plume behavior, ground-based experiments must be complemented by modeling frameworks that explicitly capture these effects. This work applies a coupled thruster-plume model to compare simulations of the H9 Hall-effect thruster operating on xenon at 300 V and 15 A in the University of Michigan's Alec D. Gallimore Large Vacuum Test Facility with those in an environment representative of Low Earth Orbit. A multi-fluid thruster model resolves plasma dynamics within the acceleration channel and near-field plume, providing boundary conditions to the plume solver. The plume model employs a hybrid kinetic-continuum approach: ion transport is treated with the particle-in-cell method, neutral transport and heavy-species collisions with the direct simulation Monte Carlo method, and electron behavior is modeled by solving fluid conservation equations. Inferred vacuum-pump sticking coefficients are incorporated to model the facility's cryogenic pumps, enabling the reproduction of experimentally validated pressure distributions in the three-dimensional chamber. Comparisons between chamber and space simulations reveal key differences relevant to spacecraft integration, emphasizing the need to account for facility effects when using chamber data to assess plume impingement on sensitive spacecraft surfaces.

Nomenclature

 N_{pairs} = Total particle pairs to be assessed for collision

 N_P = Number of macroparticles

n = Number density

 σ = Collision cross section

q = Relative velocity

t = Time

 ϵ_{coll} = Collision energy ϵ_{i} = Ionization energy ν = Collision frequency

[§]Associate Professor, Department of Aerospace Engineering



^{*}Ph.D. candidate, Ann and H. J. Smead Department of Aerospace Engineering Sciences, charles.lipscomb@colorado.edu

[†]H.T. Sears Memorial Professor, Ann and H. J. Smead Department of Aerospace Engineering Sciences

[‡]Ph.D. candidate, Department of Aerospace Engineering

 \mathbf{E} = Electric field ϕ = Electric potential \mathbf{F} = Force \mathbf{v} = Velocity

 $egin{array}{ll} \mathbf{B} &= \operatorname{Magnetic field} \\ e &= \operatorname{Elementary charge} \\ q &= \operatorname{Particle charge} \end{array}$

p = Pressure

m = Mass

 \mathbf{j} = Current density

 χ = Electrical conductivity

T = Temperature

 C_i = Ionization rate coefficient ψ = Electron velocity potential

c = Thermal speed

 k_B = Boltzmann constant κ = Thermal conductivity

 Γ = Number flux

A = Area

I. Introduction

Electric propulsion (EP) has become a cornerstone of modern spacecraft operations, particularly for orbit-raising and station-keeping missions, owing to its high specific impulse, demonstrated lifetime, and reliable performance.¹ Compared with chemical propulsion, EP thrusters achieve much greater propellant efficiency, reducing launch mass or enabling increased payload capacity. Among EP technologies, Hall-effect thrusters (HETs) are especially attractive due to their favorable thrust-to-power ratios and relatively simple design.²

The role of EP is expanding beyond station-keeping toward primary propulsion for orbital transfers. Although such transfers benefit from reduced propellant mass, they require longer maneuver durations which can be problematic. For example, human spaceflight missions demand short transfer times. High-power HETs offer a potential solution, combining efficient propellant utilization with the capability for faster transfers and large- ΔV maneuvers to support both commercial and exploration-class missions.

A central challenge to the proliferation of high-power Hall-effect thrusters is that their testing relies on ground-based vacuum facilities, whose inherent limitations distort thruster operation and plume behavior. Elevated chamber pressures alter neutral ingestion,³ increase charge-exchange ion production,⁴ and change plume divergence.⁵ Sputtered material deposition further complicates lifetime assessment,⁶ while facility walls create uncertain electrical paths that artificially modify electron transport and beam neutralization.^{7,8} These facility effects intensify with thruster power, highlighting the need for modeling frameworks that can correct or extrapolate ground data to space conditions.

Accurate prediction of EP thruster plume behavior requires boundary conditions that capture the plasma state at the thruster exit and facility models that reproduce the dynamics of background neutrals. In this work, a dedicated thruster model provides detailed plasma property predictions which are input to a plume solver through an interface in the near-field plume. Chamber background pressures are simulated through a pumping model that leverages pump-surface sticking coefficients inferred from cold-flow ionization gauge measurements. The simulation framework is applied to the magnetically shielded H9 Hall-effect thruster operating in the University of Michigan's Alec D. Gallimore Large Vacuum Test Facility (LVTF) and to the same thruster under boundary conditions representative of Low Earth Orbit (LEO).

The remainder of this paper is organized as follows. Section II outlines the numerical methods underlying the computational models. Section III presents the simulation results, compares predictions across the two environments, and discusses their implications. Finally, conclusions are given in Section IV.



II. Methods

A. Thruster and Plume Model Coupling

The coupled model integrates two simulation tools: the Hall thruster code Hall2De¹⁰ and the plume/facility code MPIC.¹¹ Hall2De provides inflow conditions to MPIC using a serial coupling framework in which data is exchanged between individual executions of the two codes. To maintain consistency between the thruster and plume simulations, the plume model adopts the same formulations for electrical conductivity, thermal conductivity, electron collision frequencies with heavy species, and heavy species collision cross sections as those used in the thruster model. Hall2De passes fluid properties for each species to MPIC along a magnetic field line interface located outside the thruster in the near-field plume. These properties include the number density, velocity, and temperature of the heavy species, as well as the electron number flux and temperature. The electric potential at the interface is also provided by the thruster model for use in the plume simulation.

The interface between the thruster and plume models is extended from the thruster exit plane into the near-field, allowing Hall2De to capture magnetic field effects prior to passing plasma flow data to MPIC. The interface traces a magnetic field line into the near-field until it becomes perpendicular to the thruster centerline, then continues along this perpendicular path to the centerline. At the intersection with the centerline, the magnetic field magnitude has decreased to less than 5% of its maximum value. The interface is discretized into azimuthally symmetric surfaces, enabling spatially varying inlet conditions to be prescribed with arbitrary resolution. In this work, 52 distinct inlet conditions are specified. The interface geometry is illustrated in Fig. 1, with the rightmost image showing the inlet numbering scheme used for plotting plume boundary condition data. The thruster model provides flow properties at nodal locations along the interface, which are linearly interpolated to face centers before being supplied to the plume model on a per-face basis.

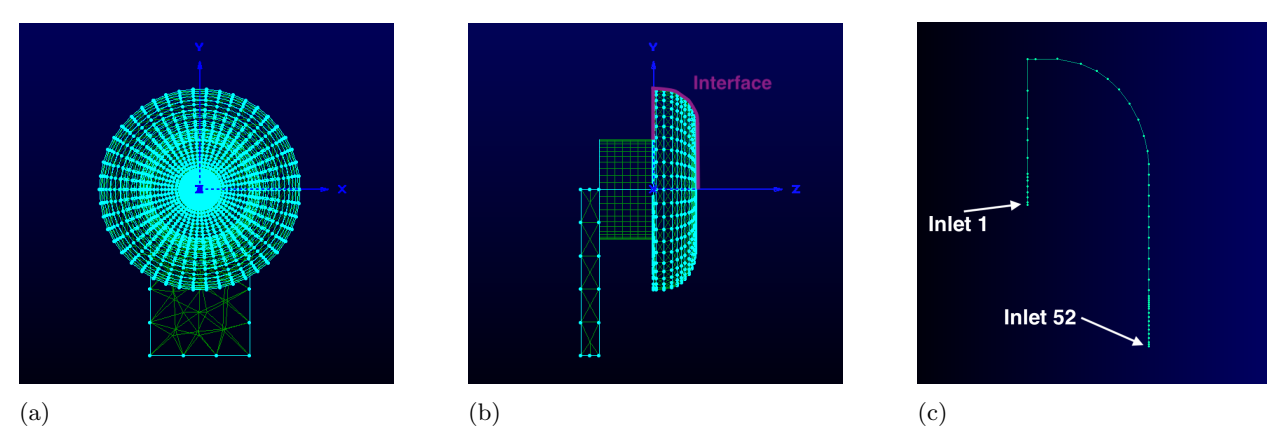


Figure 1: Front (a) and side (b) views of the interface between the thruster and plume models. The cross-sectional view (c) shows the interface with labeled inlet numbers for plotting spatially varying boundary conditions.

B. Thruster Model

Hall2De is an axisymmetric 2D multi-fluid code that simulates the channel and near-field dynamics of Hall thrusters. As detailed descriptions of the code are available in previous works, ^{10,12} only a high-level overview is provided here. Neutrals are modeled using a line-of-sight view factor algorithm that assumes neutral particles travel in straight line trajectories until they are ionized, reflected, or leave the domain. ¹³ This treatment accounts for the low collision rate of neutrals and depletion of the low energy tail due to ionization without statistical noise. Ions are modeled using the fluid continuity, momentum, and energy equations with multiple fluid populations and charge states. The multiple fluid populations account for the fact that cathode and beam ions cannot be treated as a single population due to the large difference in their bulk velocities. ¹² Ions are assigned to a fluid population based on the electrostatic potential at which they are born. A relevant limitation of the thruster model is its treatment of charge-exchange collisions. Although fast ions and slow neutrals are removed from the simulation, the corresponding reinjection of slow ions and fast neutrals is neglected.



Both the neutral and ion populations are solved on a rectilinear z-r mesh. Electron bulk properties are solved using a combination of quasi-neutrality, the generalized Ohm's law, and the internal energy equation on a magnetic field-aligned mesh. Electron cross-field transport is enhanced via inclusion of an effective "anomalous" collision frequency in addition to the ionization, Coulombic, and electron-neutral collisions. The anomalous transport in this work is specified by tuning a Bohm-like profile along the channel centerline until the model axial ion velocity profile matches experimental measurements. The electric potential is solved for by combining current conservation with the generalized Ohm's law. For the boundaries, thruster walls are accounted for with a thin sheath treatment that differentiates between conducting and insulating surfaces. Free flow boundaries are generally set via Neumann conditions with the exception of the background neutral flux and electron temperature being directly specified. Finally, the cathode inlet conditions and anode flow rate are directly specified at their respective boundary locations.

Chamber and space thruster simulations prescribe different neutral flux boundary conditions at the outflow boundaries, which specify the neutral flux entering the thruster simulation domain from the surrounding environment. For the chamber case, an ambient pressure of 5 μ Torr, measured in the University of Michigan's LVTF for the H9 HET operating at 300 V and 15 A, is assumed. From this pressure, a planar flux is computed to approximate the one-sided thermal flux of neutrals incident on a surface from a Maxwellian distribution. From kinetic theory, the one-sided flux of particles across a plane is given by:

$$\Gamma = \frac{1}{4}n\bar{v},\tag{1}$$

where Γ is the number flux, n is the number density, and \bar{v} is the mean thermal speed, given by:

$$\bar{v} = \sqrt{\frac{8k_BT}{\pi m}}. (2)$$

The number density n is computed from the ambient pressure using the ideal gas law:

$$n = \frac{p}{k_B T}. (3)$$

Substituting Eqs. 2 and 3 into Eq. 1 gives:

$$\Gamma = \frac{p}{\sqrt{2\pi m k_B T}}. (4)$$

Equation 4 computes the environmental neutral flux into the thruster domain under an assumed temperature. In space simulations, the boundary pressure is set to zero, yielding zero neutral flux at the outlets.

C. Plume and Facility Model

MPIC is a hybrid, three-dimensional plasma code that accommodates unstructured grids. The transport of neutral atoms and the collisional dynamics of all heavy species, including neutrals and ions, are modeled using the direct simulation Monte Carlo (DSMC) method. In motion is resolved with the electrostatic particle-in-cell (PIC) method, which computes self-consistent electric fields on a spatial mesh and interpolates them to particle positions. This approach captures ion acceleration under both applied and self-generated electric fields and is well suited for simulating plasma plumes from electric propulsion thrusters, where kinetic, non-equilibrium effects are significant. Since resolving electron dynamics kinetically is computationally intractable over the spatial and temporal scales considered here, electrons are treated as a fluid. Their behavior is modeled by solving conservation equations. This hybrid plasma description substantially reduces computational cost while retaining the essential physics of electron transport.

Collisions in the DSMC method are performed stochastically. Bird's No-Time-Counter scheme¹⁴ is used to calculate the total number of potential collision pairs:

$$N_{pairs} = \frac{1}{2} N_P n(\sigma g)_{max} \Delta t, \tag{5}$$

where N_P is the number of macroparticles, n is the number density, Δt is the timestep, and $(\sigma g)_{max}$ is an estimate of the maximum value of the product of the collisional cross section and the relative speed of the colliding particles within the computational cell. Whether or not a given pair collides is decided by



comparing the collision probability with a random number. The collision probability is calculated as the ratio of σq to $(\sigma q)_{max}$.

The primary collisional processes in Hall thruster plumes are momentum exchange (MEX) and charge exchange (CEX). This work models Xe-Xe MEX, Xe-Xe⁺ MEX and CEX, as well as electron-neutral and electron-ion MEX. Interactions involving Xe²⁺ and Xe³⁺ are neglected because of their low abundance. The variable hard-sphere model¹⁶ is used to determine MEX cross sections for neutral-neutral collisions. In this model, the collision cross section depends on the relative speed of the colliding particles:

$$\sigma_{\text{Xe-Xe}} = \sigma_{\text{ref}} \left(\frac{g_{\text{ref}}}{g}\right)^{2\nu},$$
 (6)

where $\sigma_{\rm ref}$ is the reference cross section, q is the relative velocity, and ν is a species-dependent exponent that controls the temperature dependence of the viscosity. The reference cross section is computed using the hard-sphere formula:

$$\sigma_{\rm ref} = \pi d_{\rm ref}^2,\tag{7}$$

where d_{ref} is the reference diameter. Table 1 lists the VHS parameters used for all species in this study, ¹⁴ including oxygen to represent the Low Earth Orbit freestream. The value of ν for Xe-O collisions is taken to be the average from the Xe-Xe and O-O collisions in the absence of a measured value.

Table 1: Variable hard sphere model parameters for relevant species pairs.

ion Pair	Viscosity Index, ν	Reference Temperature,	Reference Diameter,
		$T_{\rm ref}$ (K)	d_{ref} (m)

Collisio 5.74×10^{-10} Xe-Xe 0.35 273.0 3.00×10^{-10} O-O0.27273.0273.0 4.37×10^{-10} Xe-O 0.31

CEX collisions are indispensable in HET plume models due to the population of slow atoms and fast ions in the near-field plume.¹⁷ The ions in this region have been electrostatically accelerated and have significantly greater velocities than the atoms, which move at thermal speeds, by approximately two orders of magnitude. 18 The code simulates CEX collisions with the understanding that CEX is a subset of atom-ion MEX collisions. The cross section for atom-ion CEX and MEX is modeled using measured data¹⁹ which yields the following semi-empirical formula:

$$\sigma_{\text{Xe-Xe}^+} = 10^{-20} \left(87.3 - 13.6 \log_{10}(\epsilon_{coll}) \right),$$
 (8)

where ϵ_{coll} is the collision energy in eV. Unlike simpler models that assume isotropic scattering, the approach used in this work resolves anisotropic scattering by computing differential cross sections from interatomic potentials. This method, adopted from the work by Katz et al.²⁰ and Boyd & Dressler, ¹⁸ offers a more accurate description of Xe-Xe⁺ collisions by directly accounting for the underlying physics of momentum and charge exchange.

The PIC model employs the electrostatic approximation, which assumes that time-varying magnetic fields are negligible. Under this assumption, the electric field can be expressed as the negative gradient of a scalar electric potential:

$$\mathbf{E} = -\nabla \phi. \tag{9}$$

where **E** is the electric field and ϕ is the potential. This formulation eliminates the need to solve Maxwell's equations in full. The dynamics of ions in the plume are governed by the Lorentz force:

$$\mathbf{F} = q(\mathbf{E} + \mathbf{v} \times \mathbf{B}),\tag{10}$$

where q is the particle charge, v is the velocity, and B is the magnetic field. The $\mathbf{v} \times \mathbf{B}$ term is neglected, as Hall thruster ions are effectively unmagnetized due to their large gyroradii, especially in the plume where magnetic fields are weak.



The electron model, referred to as the Detailed electron model, solves electron fluid conservation equations. The Detailed model starts with the steady-state electron momentum conservation equation, neglecting advection and magnetic field effects:

$$0 = -n_e e \mathbf{E} - \nabla p_e + m_e n_e (\mathbf{v_i} - \mathbf{v_e}) \nu_{ei}. \tag{11}$$

Here, e is the elementary charge, p_e is the electron pressure, m_e is the electron mass, $\mathbf{v_i}$ is the ion velocity, $\mathbf{v_e}$ is the electron velocity, and ν_{ei} is the electron-ion collision frequency. Assuming quasineutrality allows for the substitution of the current density, $\mathbf{j} = \mathbf{j_i} + \mathbf{j_e} = e * n_e(\mathbf{v_i} - \mathbf{v_e})$, within the friction term. The result is:

$$0 = -n_e e \mathbf{E} - \nabla p_e + \frac{m_e \nu_{ei}}{n_e e^2} \mathbf{j}.$$
 (12)

Substituting the electrical conductivity, $\chi = \frac{n_e e^2}{m_e \nu_e}$, and solving for the current density results in the generalized Ohm's Law:

$$\mathbf{j} = \chi \mathbf{E} + \frac{\chi}{n_e e} \nabla p_e. \tag{13}$$

Substituting Eq. 13 into the charge continuity equation, $\nabla \cdot \mathbf{j} = 0$, and using Eq. 9 along with the ideal gas law yields the momentum equation of the Detailed electron model:

$$\nabla \cdot \left(-\chi \nabla \phi + \frac{\chi k_B}{n_e e} \nabla (n_e T_e) \right) = 0. \tag{14}$$

This equation depends on the electron temperature which is calculated from the steady state electron energy equation, presented in Eq. 20, whose derivation may be found in Ref. 21. The energy equation is dependent upon the electron velocity, necessitating the solution of the electron continuity equation. The continuity equation is:

$$\frac{\partial}{\partial t}(n_e) + \nabla \cdot (n_e \mathbf{v_e}) = n_e n_a C_i, \tag{15}$$

where C_i is the ionization rate coefficient. C_i is modeled using the relation from Ahedo et al.:²²

$$C_i = \sigma_{ref} c_e \left(1 + \frac{T_e \epsilon_i}{(T_e + \epsilon_i)^2} \right) exp \left(\frac{-\epsilon_i}{T_e} \right), \tag{16}$$

where c_e is the electron thermal speed and ϵ_i is the ionization energy. Assuming the electrons are irrotational allows one to define an electron velocity potential function, ψ :

$$\nabla \psi = n_e \mathbf{v_e}.\tag{17}$$

Assuming steady state and substituting Eq. 17 into Eq. 15 reaps the final form of the continuity equation. The fluid electron conservation equations for mass, momentum, and energy that define the Detailed electron model are expressed below.

$$\nabla^2 \psi = n_e n_n C_i \tag{18}$$

$$\nabla \cdot (\chi \nabla \phi) = \frac{k_B}{q} \left(\chi \nabla^2 T_e + \chi T_e \nabla^2 \ln(n_e) + \chi \nabla \ln(n_e) \cdot \nabla T_e + T_e \nabla \chi \cdot \nabla \ln(n_e) + \nabla \chi \cdot \nabla T_e \right)$$
(19)

$$\nabla^{2}T_{e} = -\nabla \ln(\kappa) \cdot \nabla T_{e} + \frac{1}{\kappa} \left(-\mathbf{j}_{e} \cdot \mathbf{E} + \frac{3}{2} n_{e} (\mathbf{v}_{e} \cdot \nabla) k_{B} T_{e} + p_{e} \nabla \cdot \mathbf{v}_{e} \right)$$

$$+ \frac{1}{\kappa} \left(\frac{3m_{e}}{m_{h}} \nu_{e} n_{e} k_{B} (T_{e} - T_{h}) + n_{e} n_{h} \epsilon_{i} C_{i} \right)$$

$$(20)$$

The transport coefficients are calculated as:

$$\chi = \frac{n_e e^2}{m_e \nu_e} \tag{21}$$

$$\kappa_e = 3.16 \frac{k_B^2 n_e T_e}{m_e \nu_e} \tag{22}$$

where χ is the electrical conductivity, κ is the thermal conductivity, and ν_e is the total electron collision frequency with heavy species. Expressions for electrical conductivity and thermal conductivity are taken from Refs. 21 and 23, respectively. Equation 18 yields the electron velocity, Eq. 19 yields the electric potential, and Eq. 20 yields the electron temperature.



III. Results

A. Thruster Model Results

The thruster model used in this work is capable of simulating multiple fluid populations to represent distinct ion groups within a given species. This capability is leveraged to improve the fidelity of ion dynamics by enabling the resolution of multiple Maxwellian velocity distributions. In contrast, a single-fluid approach requires all ions of a given charge state to conform to a single Maxwellian distribution, which oversimplifies the range of ion velocities observed in the plasma.

In this study, ions are sorted into four separate fluid populations for each charge state based on the electrostatic potential at the location where they become ionized. This multi-fluid strategy approximates the underlying energy spread in the plasma without incurring the computational cost of a fully kinetic method like PIC. The potential bins are: above 317 V, 310–317 V, 50–310 V, and below 50 V, corresponding to populations 1 through 4, respectively. These bins are selected to ensure that each population contributes approximately equally to the total ion current at the far-field axial boundary, thereby balancing numerical resolution across the spectrum of ion energies.

Figure 2 presents spatial distributions of plasma properties in the near-field from a Hall2De simulation of the H9 HET operating on xenon at 300 V and 15 A. The ion data shown correspond to the first fluid population of singly charged xenon ions, defined by their creation in regions where the local electrostatic potential exceeds 317 V. The ion number density exhibits a high-density region along the radial axis at the acceleration channel exit and a second along the thruster centerline, formed by the convergence of flow from the azimuthally symmetric annulus. Axial velocity contours show peak values exceeding 20 km/s along the centerline, with velocities decreasing radially outward. This distribution reflects ion acceleration by the axial electric field established in the discharge channel and near-field plume. The compactness of the velocity contours near the thruster exit indicates that most of the potential drop occurs within a short axial distance of the exit plane, defining the primary ion acceleration zone. Together, these results highlight key features of Hall thruster near-field behavior. They include a dense high-velocity ion core, steep axial electric fields at the channel exit, and smooth plume expansion downstream.

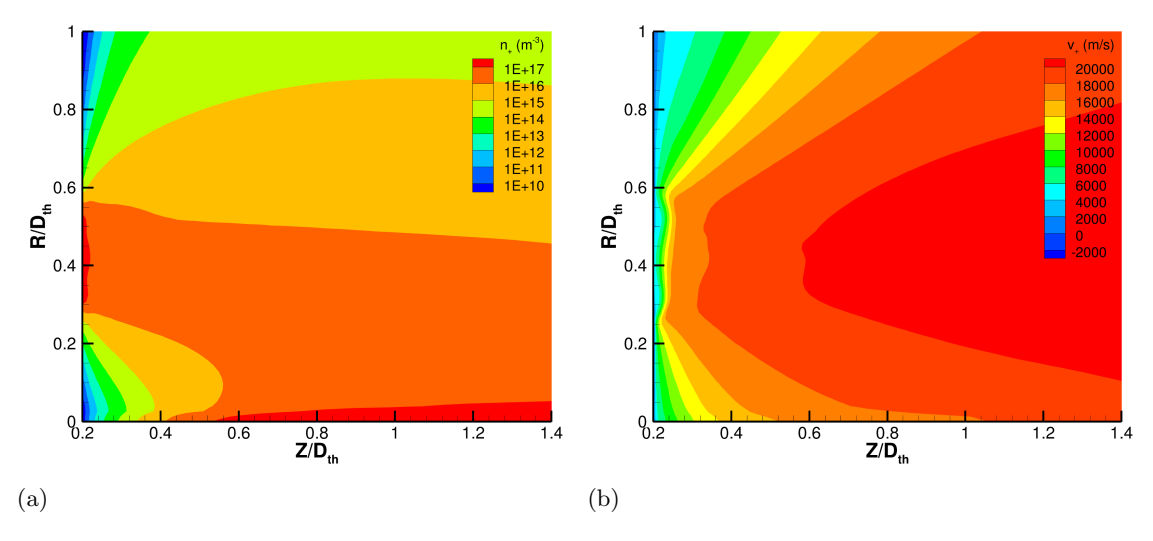


Figure 2: Hall2De solution for the H9 HET operating on xenon at 300 V and 15 A: (a) population-1 singly charged ion number density and (b) population-1 singly charged ion axial velocity. All spatial coordinates are normalized by the thruster diameter, $D_{\rm th}$.

B. Plume Model Boundary Conditions

The differences between space and chamber simulations arise from the boundary conditions applied to the thruster and plume models. Plasma plume simulations of the H9 HET are performed using conditions representative of both Michigan's Large Vacuum Test Facility and a typical Low Earth Orbit environment. In the chamber case, plume expansion is constrained by physical walls, whereas in space it develops into open, non-confining boundaries. The chamber simulations incorporate previously inferred sticking coefficients to



represent the two types of vacuum pumps populating Michigan's chamber. The sticking coefficient specifies the fraction of particle–pump interactions that result in adsorption rather than reflection. A sticking coefficient of 0.26 is applied to the PHPK-TM1200i re-entrant cryopumps, and a value of 0.22 is applied to the University of Michigan—designed liquid-nitrogen-free cryosails.²⁴ A schematic of the pumping surfaces is provided in Fig. 3, and a detailed description of the pressure model and methodology for inferring sticking coefficients is available in Ref. 9.

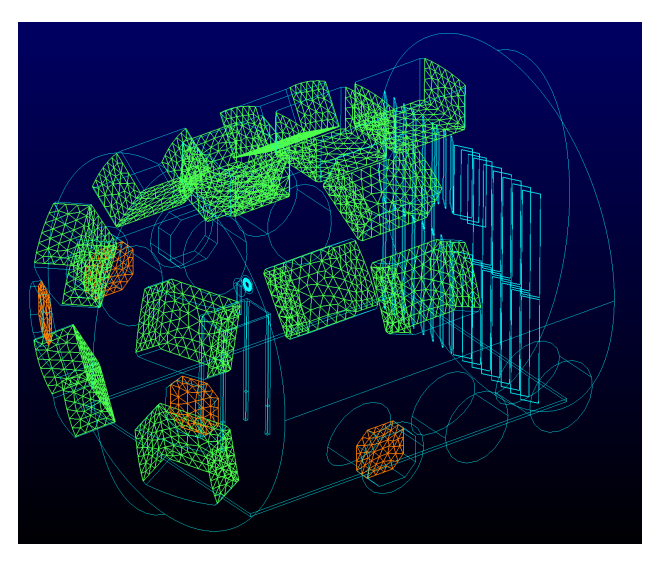


Figure 3: Configuration of the two vacuum pump types in Michigan's Large Vacuum Test Facility. Cryopump surfaces are indicated in green, and cryosail surfaces in orange.

Figures 4–9 compare the inlet boundary conditions supplied by the thruster model to the plume model for chamber and space simulations. Differences at the thruster–plume interface are generally minor. As expected, the space simulation predicts lower neutral densities and more positive axial/radial velocities due to reduced backpressure. In both simulations, the neutral population is modeled as being emitted from the thruster surfaces at a uniform temperature of 773 K. Ion number densities are broadly consistent across environments, with the largest discrepancy near the axis of symmetry (inlet 52), where reduced ion scattering from background neutrals in space produces higher density. Ion velocities differ only modestly, suggesting that the electrostatic potential profile is not significantly different between the two cases for the purposes of ion acceleration. Ions are generally predicted to have higher temperatures in the space simulation than in the chamber simulation, reflecting reduced scattering with background neutrals that would otherwise cool and randomize ion velocities. Electron properties, shown in Fig. 9, exhibit slightly higher potentials in the chamber case, while electron number flux and temperature remain nearly identical between the two environments. Inlet properties for doubly and triply charged ions may be found in the Appendix.

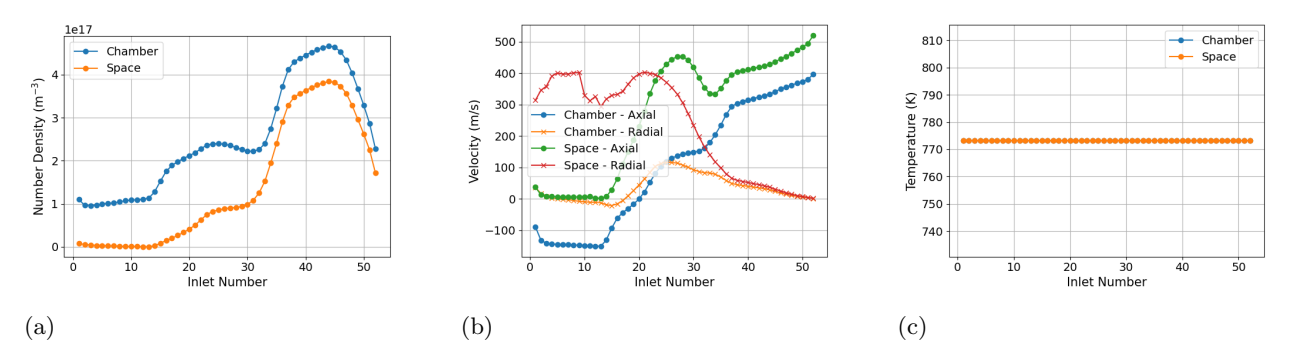


Figure 4: Profiles of Xe properties across the thruster–plume interface: (a) number density, (b) velocity components, and (c) temperature, shown for both chamber and space simulations. These quantities are supplied by the thruster model as boundary conditions for the plume model. Please see Fig. 1 for inlet numbering information.

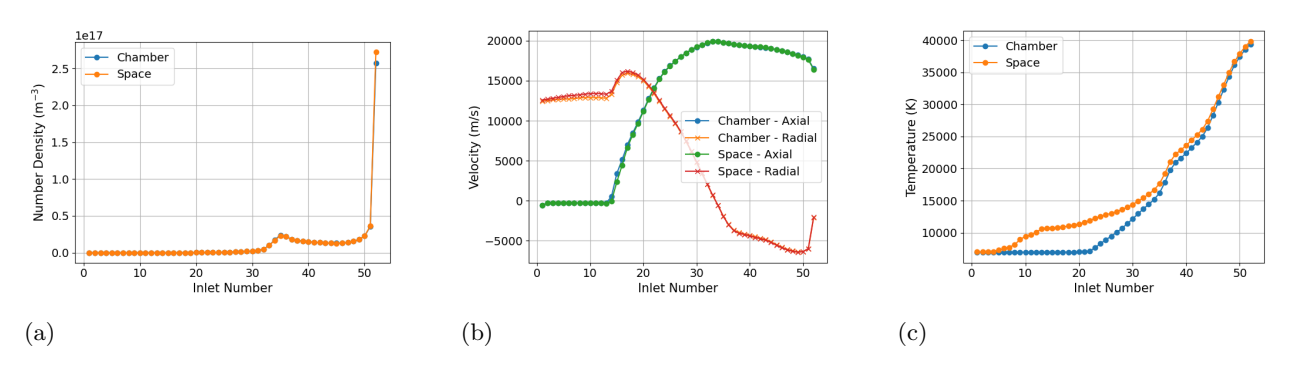


Figure 5: Profiles of Xe⁺ population 1 properties across the thruster–plume interface: (a) number density, (b) velocity components, and (c) temperature, shown for both chamber and space simulations.

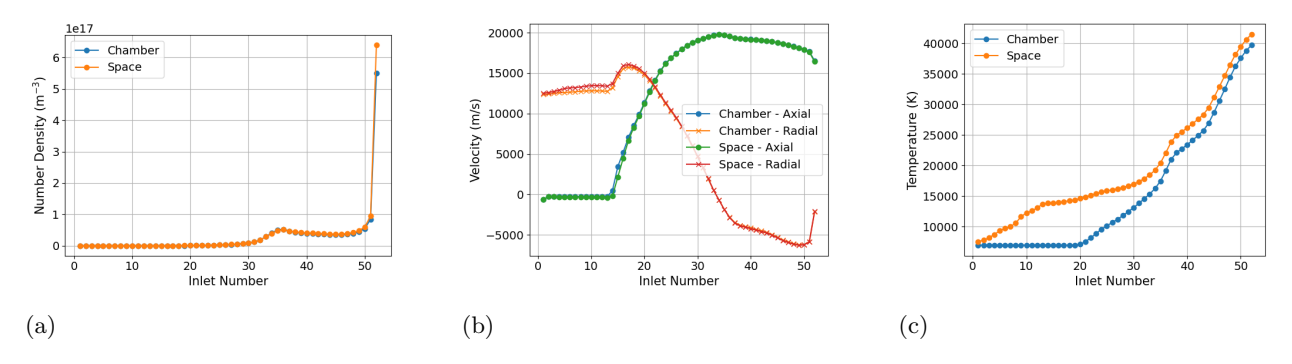


Figure 6: Profiles of Xe⁺ population 2 properties across the thruster–plume interface: (a) number density, (b) velocity components, and (c) temperature, shown for both chamber and space simulations.

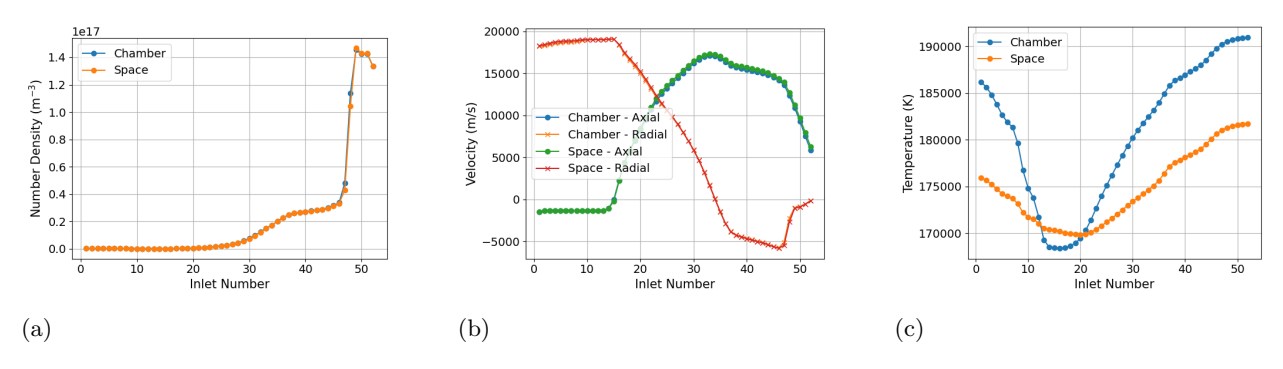


Figure 7: Profiles of Xe⁺ population 3 properties across the thruster–plume interface: (a) number density, (b) velocity components, and (c) temperature, shown for both chamber and space simulations.

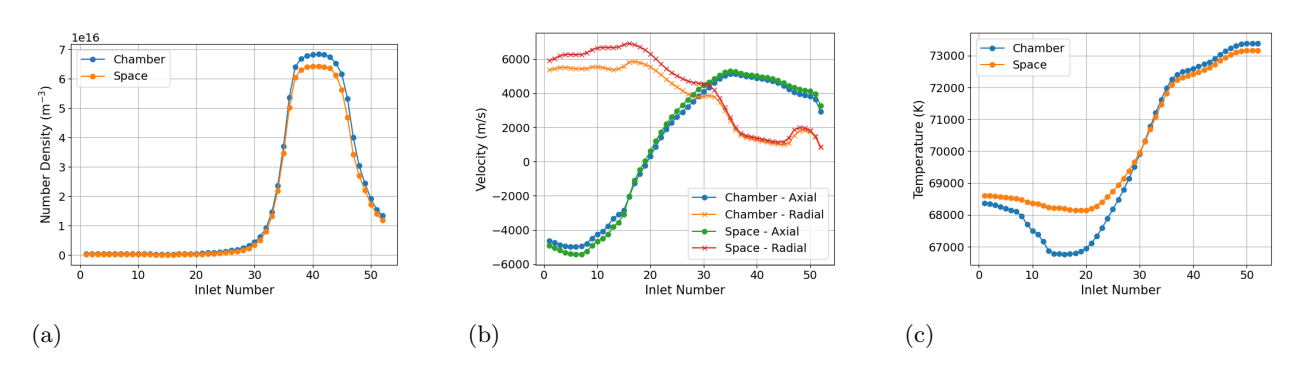


Figure 8: Profiles of Xe⁺ population 4 properties across the thruster-plume interface: (a) number density, (b) velocity components, and (c) temperature, shown for both chamber and space simulations.

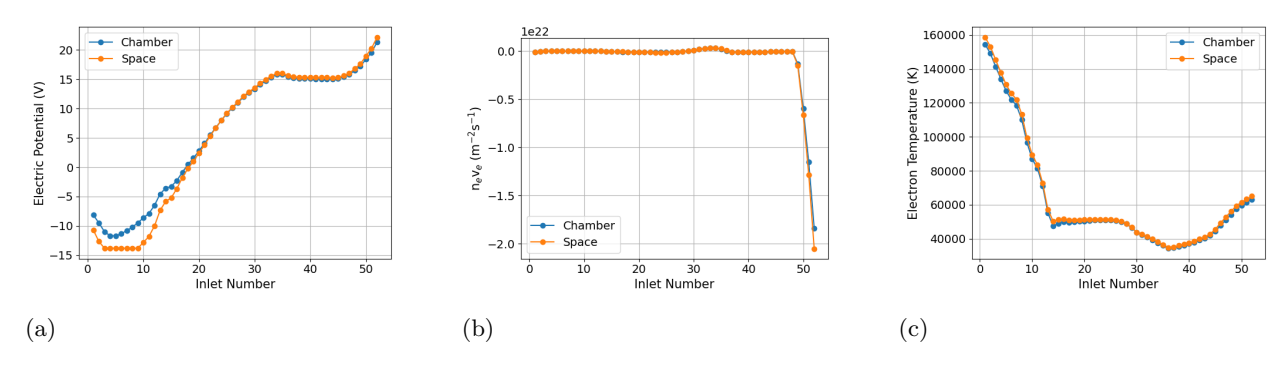


Figure 9: Profiles of key plasma properties across the thruster–plume interface: (a) electric potential, (b) electron flux, and (c) electron temperature, shown for both chamber and space simulations.

The spacecraft surface on which the HET is mounted is modeled with an accommodation coefficient of 1.0, a sticking coefficient of 0.0, and a surface temperature of 300 K, consistent with the values applied to the internal chamber walls. Boundary conditions for the Detailed electron model are summarized in Tables 2 and 3, corresponding to the chamber and space simulations, respectively. The primary differences between the two environments are the potentials applied to the thruster body and outer boundaries, as well as the electron temperature specified at the outer boundaries.

In the space simulation, we apply a Neumann zero condition at the outflow boundaries, enforcing zero normal electric field at the domain edges. This choice is justified by the decay of the electric field with distance from the thruster and by the fact that the simulation domain extends many thruster diameters in both axial and radial directions. A Neumann zero condition is also applied to the electron temperature at the outflow boundaries, consistent with the assumption of negligible plasma-property gradients far from the



thruster. In contrast, the chamber simulation imposes zero potential at the walls to represent the grounded chamber surfaces. An electron temperature of 1 eV is assigned to the chamber walls, following values adopted in previous studies. 25,26

The spacecraft potential in Low Earth Orbit is determined by enforcing a zero-current condition. A conducting body exposed to unequal ion and electron fluxes accumulates a net charge. In Low Earth Orbit at an altitude of 400 km, the ion thermal velocity is smaller than the orbital velocity, which is itself smaller than the electron thermal velocity. Consequently, ions strike only those surfaces oriented in the direction of motion. The ion current is:

$$I_i = e n_0 v_0 A_i, \tag{23}$$

where e is the elementary charge, n_0 is the ambient ion number density, v_0 is the orbital velocity, and A_i is the effective area of the spacecraft collecting ions. The electron current is:

$$I_e = \frac{1}{4}en_0 \exp\left(\frac{e\phi_{sc}}{k_B T_e}\right) v_{e,th} A_{sc},\tag{24}$$

where ϕ_{sc} is the spacecraft potential, $v_{e,th}$ is the electron thermal velocity, T_e is the electron temperature, and A_{sc} is the total surface area of the spacecraft. The spacecraft charges negatively until the potential is sufficient to repel excess electrons and balance the ion and electron currents. Setting Eqs. 23 and 24 equal yields the floating potential:

$$\phi_{sc} = \frac{k_B T_e}{e} \ln \left(\frac{4v_0 A_i}{v_{e,th} A_{sc}} \right). \tag{25}$$

For an electron temperature of $T_e = 0.1$ eV and assuming $A_i/A_{sc} = 1/2$, the resulting spacecraft potential is $\phi_{sc} = -0.3$ V, which is the value used in the LEO plume simulations. In the chamber case, the thruster body potential is set to an experimentally measured value. For the LEO case, freestream conditions corresponding to an altitude of 400 km are used. The properties of the atomic oxygen freestream particles are listed in Table 4. The freestream velocity is aligned with the thruster exhaust direction.

Table 2: LVTF Detailed fluid-electron boundary conditions (excluding thruster inlet).

Boundary	$\psi \ (m^{-1}s^{-1})$	φ (V)	T_e (eV)
Thruster Body	Neumann 0.0	Dirichlet -18.6	Dirichlet 1.0
Chamber Walls	Dirichlet 0.0	Dirichlet 0.0	Dirichlet 1.0

Table 3: LEO Detailed fluid-electron boundary conditions (excluding thruster inlet).

Boundary	$\psi \ (m^{-1}s^{-1})$	ϕ (V)	T_e (eV)
Thruster Body / Spacecraft	Neumann 0.0	Dirichlet -0.3	Dirichlet 1.0
Outflow	Dirichlet 0.0	Neumann 0.0	Neumann 0.0

Table 4: LEO Ambient Flow Conditions.²⁷

Species	$m \text{ (kg kmol}^{-1})$	T (eV)	$v \; ({\rm m} \; {\rm s}^{-1})$	$n ({\rm m}^{-3})$
О	16.0	0.06	7640	9.3×10^{13}

C. Plume Model Results

Slices of the three-dimensional grids used to represent the space and chamber environments are shown in Fig. 10. The grid resolution is chosen such that cell sizes remain smaller than the minimum local mean free path of the heavy species, ensuring accurate treatment of collisions. The Debye length does not constrain the mesh in this work, as quasineutrality is assumed. The plume simulations contain approximately 20



million particles at steady state, distributed across a computational domain comprised of about 500,000 tetrahedral cells. This corresponds to an average of 40 particles per cell. Steady state is achieved after simulating 3 seconds of physical time. Once steady state is reached, macroscopic quantities are sampled over 190,000 iterations, with data recorded at every iteration. The minimum local mean collision time in the flow, 5×10^{-7} s, is adopted as the simulation timestep.

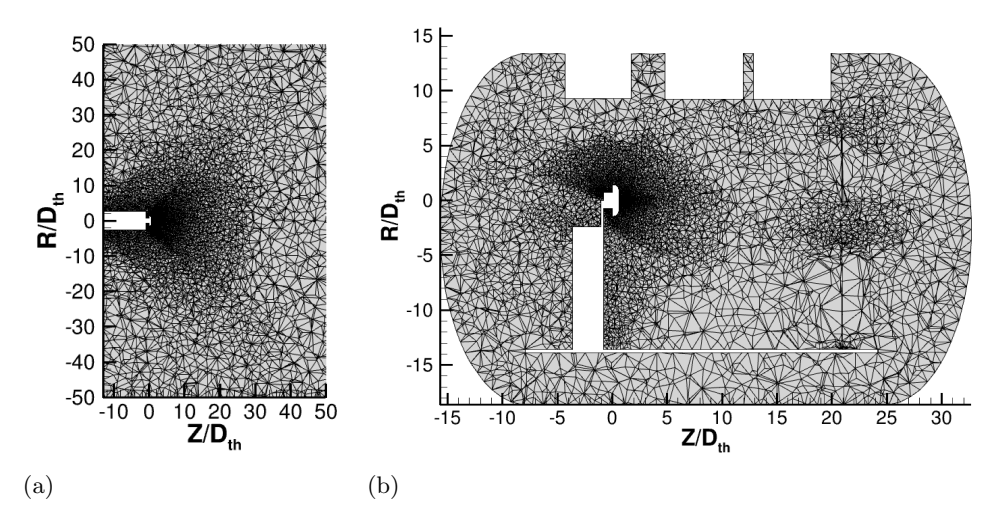


Figure 10: Two-dimensional slices of the three-dimensional computational grids: (a) domain used for plasma flow simulation in LEO and (b) domain used for simulation in the LVTF.

Results comparing the chamber and space plume simulation predictions are presented in Figs. 11–20. The coordinate origin is defined as the intersection of the thruster centerline and the exit plane. Figure 11 shows neutral number density contours, which reveal the expected depletion of neutrals in the space simulations compared with the chamber case. In the space environment, neutral densities only reach 1×10^{17} m⁻³ immediately in front of the thruster, whereas in the chamber they remain above this value throughout the entire domain. Figure 12 presents neutral velocity contours. In the space simulation, axial velocities are significantly higher due to the absence of thermalized background gas. In contrast, the chamber environment contains a substantial population of thermalized neutrals produced by repeated wall interactions, which act to randomize the average neutral motion and suppress directed velocity. These results underscore how chamber effects alter both the magnitude and character of the neutral flow field.

Figure 13 shows that singly charged ions are more abundant upstream of the thruster exit plane in the chamber simulations than in the space simulations. The elevated upstream ion population results from increased charge-exchange interactions, coupled with the influence of grounded chamber walls, which generate electric fields that bend ion trajectories back behind the thruster. As illustrated in Figs. 14 and 16, the highest axial ion velocities in the chamber remain confined to narrower regions than in space. This confinement reflects the restricted plume expansion and the reduced far-field potential drop imposed by the chamber boundaries. The distributions of doubly charged ion number densities, shown in Fig. 15, are qualitatively similar in both environments, likely because collisions for higher charge states are not modeled in this work. Contours of triply charged ion properties are provided in the Appendix for completeness.

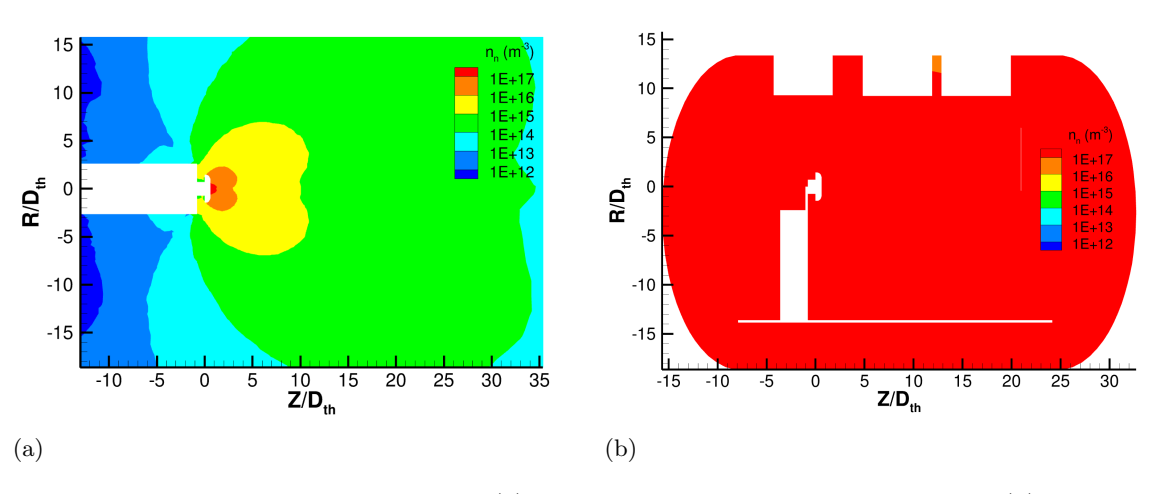


Figure 11: Neutral number density contours: (a) simulation of the H9 HET in LEO and (b) simulation in the LVTF.

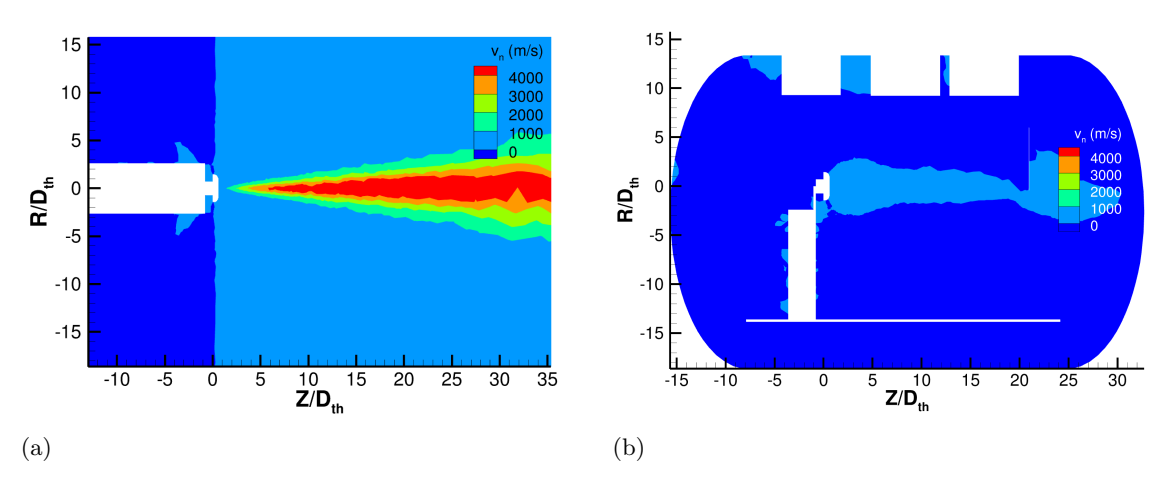


Figure 12: Neutral axial velocity contours: (a) simulation of the H9 HET in LEO and (b) simulation in the LVTF.

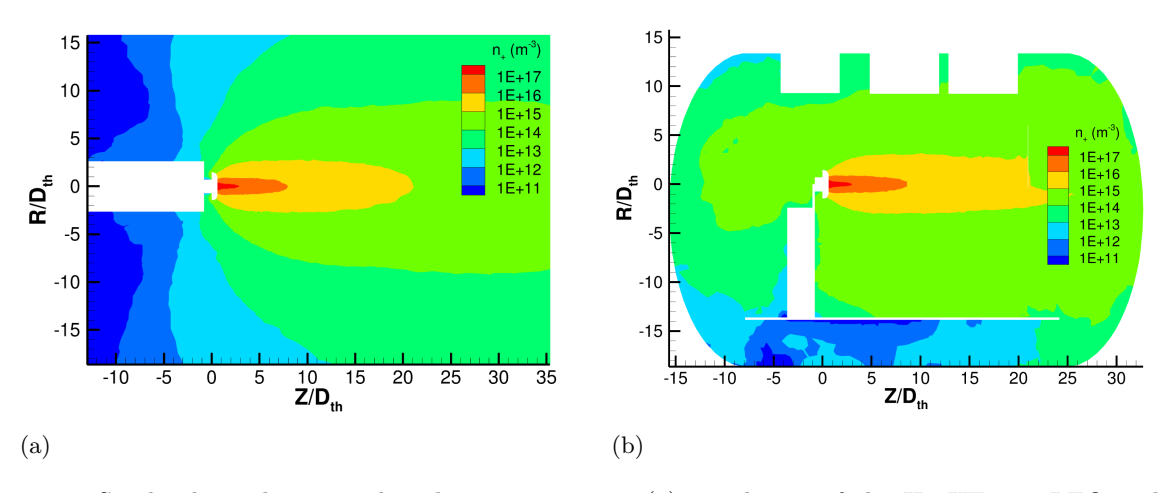


Figure 13: Singly charged ion number density contours: (a) simulation of the H9 HET in LEO and (b) simulation in the LVTF.



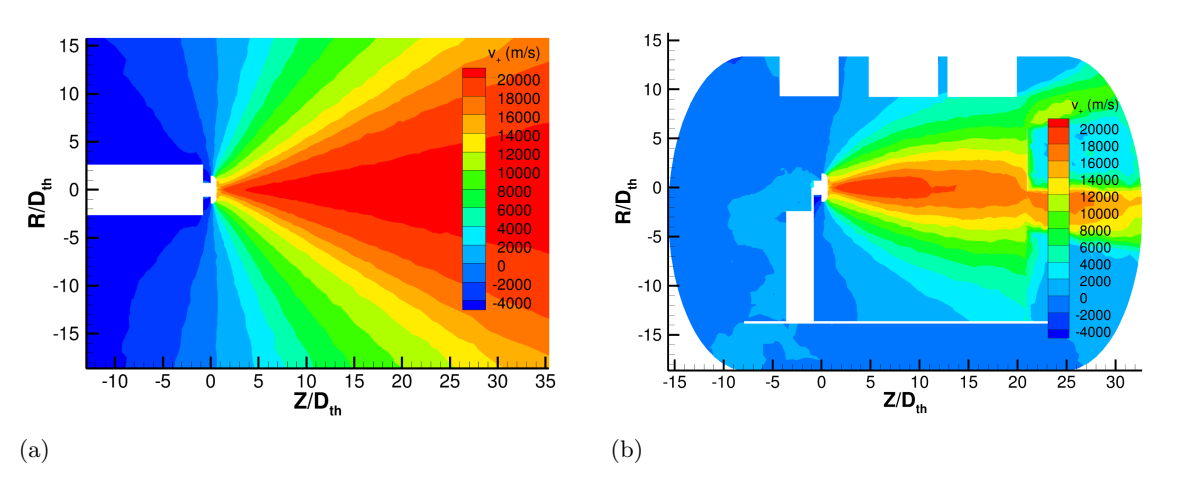


Figure 14: Singly charged ion axial velocity contours: (a) simulation of the H9 HET in LEO and (b) simulation in the LVTF.

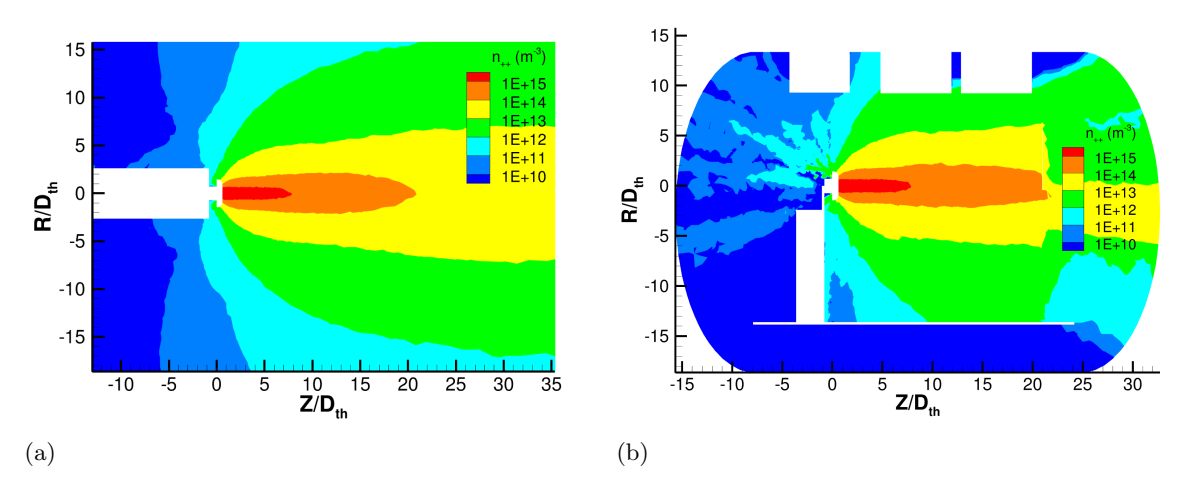


Figure 15: Doubly charged ion number density contours: (a) simulation of the H9 HET in LEO and (b) simulation in the LVTF.

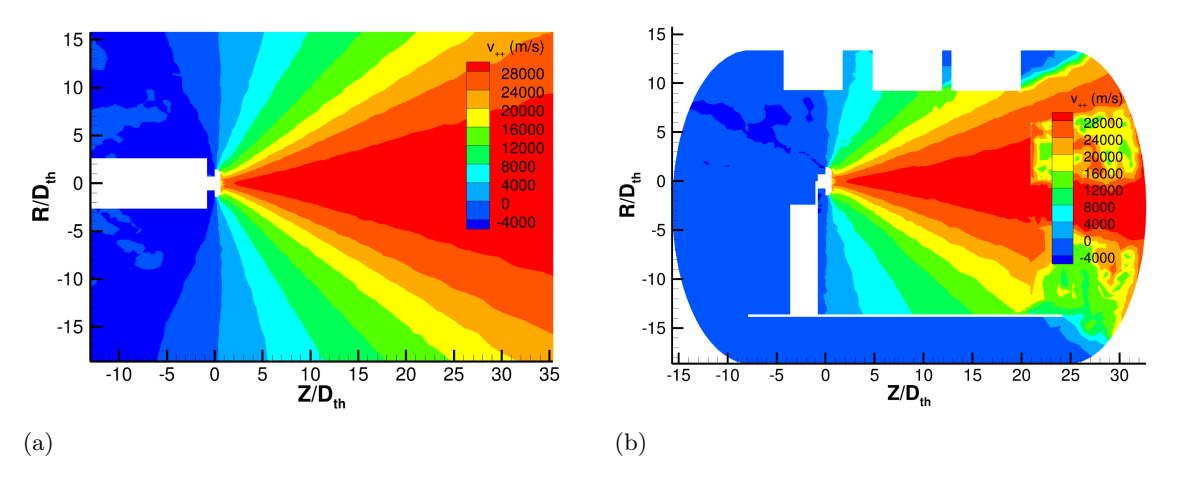


Figure 16: Doubly charged ion axial velocity contours: (a) simulation of the H9 HET in LEO and (b) simulation in the LVTF.



Figure 17 presents contours of electron axial velocity, revealing clear differences between the chamber and space simulations. Although the overall flow structure is similar, the space simulations predict that electrons sustain high axial velocities farther from the thruster. In contrast, the chamber simulations produce more contracted contours, with elevated electron speeds confined to the near-field plume. Figure 18 shows broadly similar electron temperature contours in both environments. The lowest contour (2 eV), however, appears in the space simulation only in a small region behind the thruster near the spacecraft appendage, whereas in the chamber it occupies most of the domain and forms once the plume reaches the far field. The electric potential distributions in Fig. 19 differ much more dramatically, as the grounded chamber walls constrain the potential field, halting its natural decay and thereby modifying the downstream acceleration of ions.

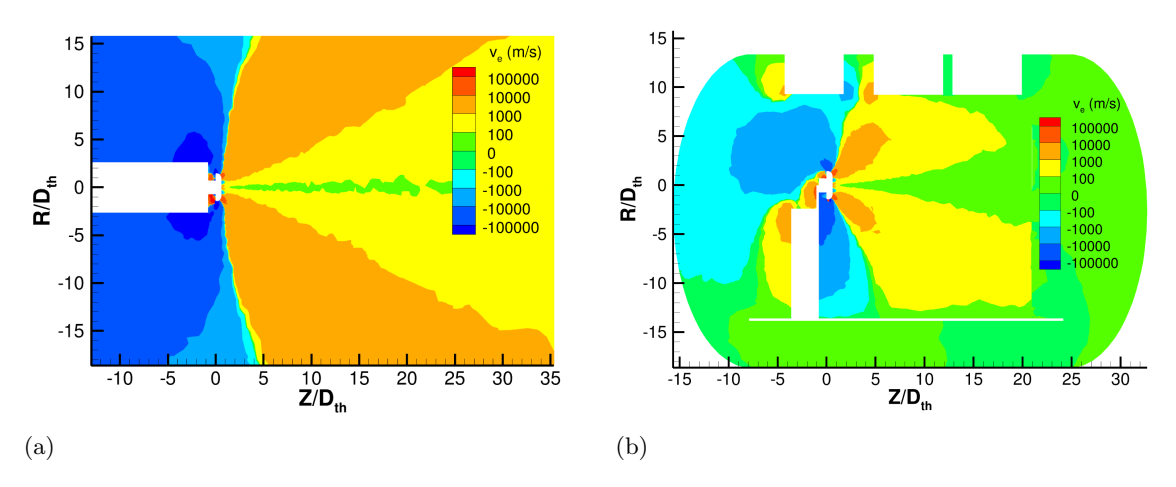


Figure 17: Electron axial velocity contours: (a) simulation of the H9 HET in LEO and (b) simulation in the LVTF.

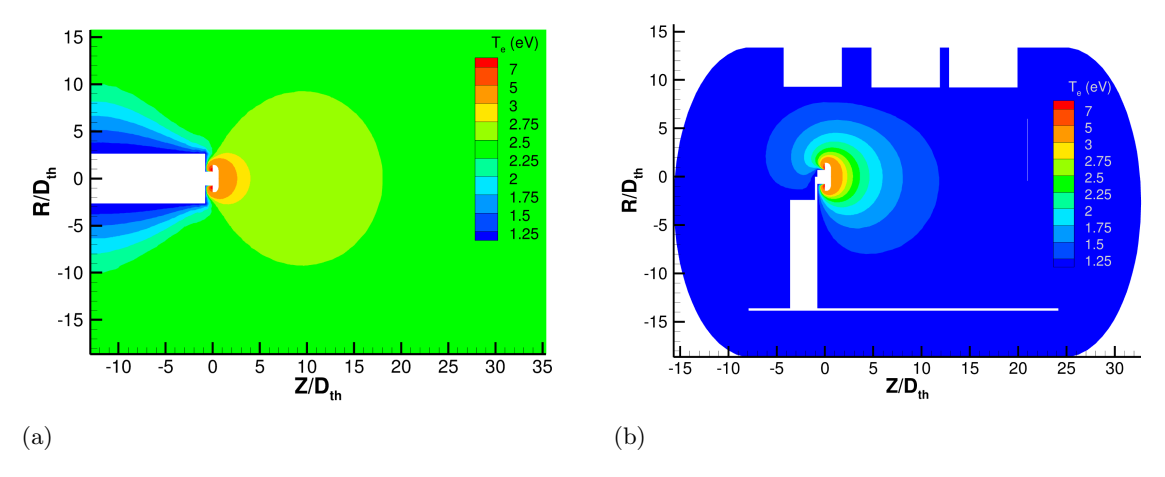


Figure 18: Electron temperature contours: (a) simulation of the H9 HET in LEO and (b) simulation in the LVTF.

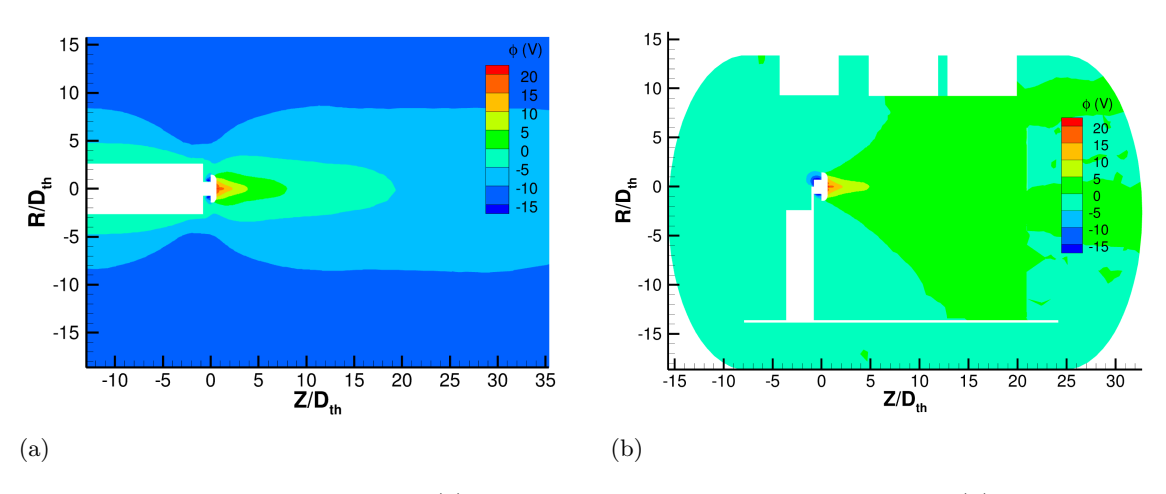


Figure 19: Electric potential contours: (a) simulation of the H9 HET in LEO and (b) simulation in the LVTF.

Figure 20 presents contours of charge—exchange collision frequencies per unit volume, clearly illustrating the much higher levels of charge—exchange activity in the chamber relative to space. In the space simulation, charge—exchange events are concentrated in a narrow region immediately downstream of the thruster, reflecting the rapid depletion of neutrals in the open domain. By contrast, in the chamber simulation charge—exchange activity extends throughout the entire simulated volume, sustained by elevated background neutral densities. These results emphasize the role of facility effects in artificially enhancing ion—neutral interactions and highlight the importance of accounting for such processes when extrapolating chamber data to space conditions.

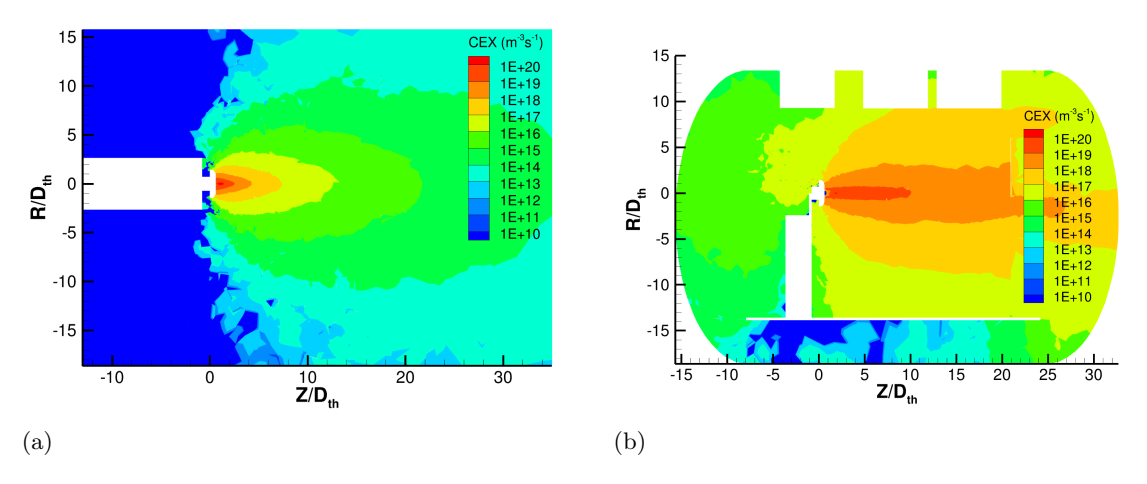


Figure 20: Charge-exchange collision frequency density contours: (a) simulation of the H9 HET in LEO and (b) simulation in the LVTF.

Figure 21 compares ion current density predictions from the chamber and space simulations at a distance of 1.32 m from the thruster center. Over most of the angular sweep, the chamber and space simulations yield nearly identical current density profiles, indicating that the beam-directed ion populations are largely unaffected by facility effects. The profiles begin to diverge near 85° off the thruster centerline and separate sharply around 110°. Beyond this point, the chamber simulation predicts ion current densities roughly two orders of magnitude greater than those in space, and this elevated level persists out to the largest recorded angle. This behavior is directly linked to the enhanced charge—exchange activity in the chamber environment (see Fig. 20). The abundance of slow, electrically mobile charge—exchange ions in the chamber raises the ion current density at large angles, whereas in space the lower neutral density and reduced charge—exchange frequency cause the ion current density to fall off more rapidly, yielding a narrower and more collimated ion distribution.



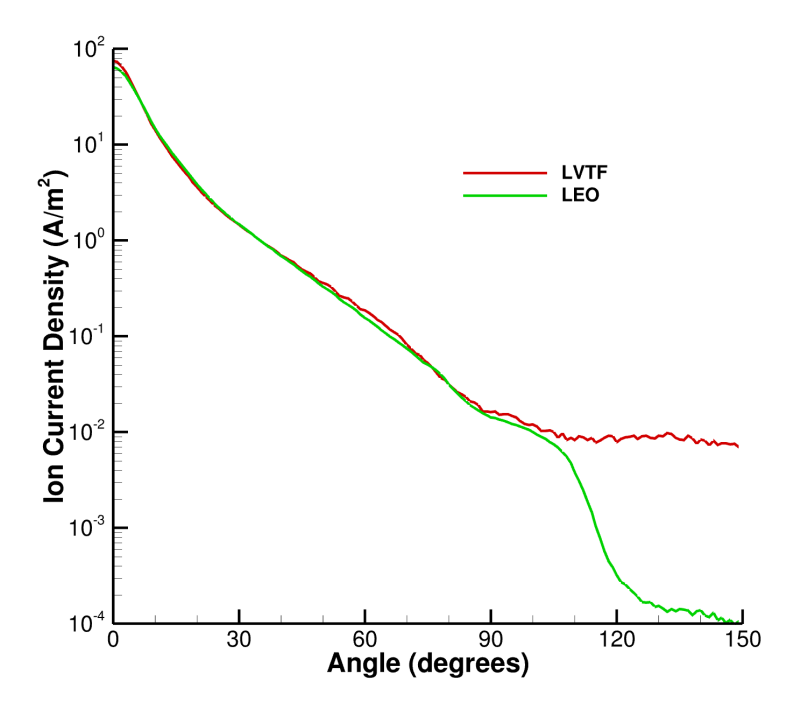


Figure 21: Comparisons between ion current density predictions from simulations in the LVTF and LEO. The ion current density results are from an angular sweep 1.32 m from the thruster center.

Figure 22 compares simulated ion energy distributions along the thruster centerline for the chamber and space environments at a distance of 1.64 m from the thruster exit plane. In the chamber case, a pronounced peak appears in the lowest energy bins, caused by slow ions generated through charge-exchange collisions with the background gas. A similar but much smaller feature is present in the space simulation, reflecting the much lower neutral density in that environment. The ion energy distributions were obtained by numerically differentiating the simulated retarding potential analyzer I–V characteristic using a finite-difference scheme. Because the I–V trace exhibits a sharp drop near zero retarding potential, the derivative amplifies this discontinuity and produces the dramatic spike observed in the first two bins. Results are plotted with both full-scale and zoomed y-axis limits to reveal lower-amplitude features. Future work will implement a more robust method that directly tallies ions into energy bins rather than relying on numerical differentiation of the I–V curve.

Simulations of both environments produce peaks near the expected beam energy, 300 V, indicating that the core acceleration mechanism is preserved. The chamber distribution, however, is shifted slightly toward lower energies relative to the space case. This shift results from the grounded chamber walls, which prevent the potential from dropping below zero and thereby halt electrostatic acceleration in the far-field. In contrast, the space simulation allows the potential to continuously decay, enabling ions to gain additional energy downstream. The LEO distribution also appears somewhat broader, consistent with the more extended far-field acceleration region in space.

This work also quantifies the neutral flux entering the thruster near field as a means of characterizing the backpressure facility effect. Figure 23 defines the thruster model boundaries across which the neutral flux from the plume domain into the near-field region is computed. The resulting values for both chamber and space environments are presented in Table 5. The results reveal a marked disparity between the two cases. In the chamber, all three neutral flux predictions are on the order of 10^{18} particles m⁻² s⁻¹, a consequence of the high background neutral densities sustained by recirculation from the chamber walls. By comparison, the space simulation yields neutral fluxes several orders of magnitude lower. In particular, the "Forward Axial Flux" of neutrals is nearly five orders of magnitude smaller in space than in the chamber. These results demonstrate how chamber effects produce relatively large artificial neutral fluxes into the thruster near-field, which in turn alter ingestion, charge–exchange production, and plume divergence relative to the space environment. Incorporating these neutral flux values into a thruster model to assess their impact on predicted performance and lifetime is reserved for future work.



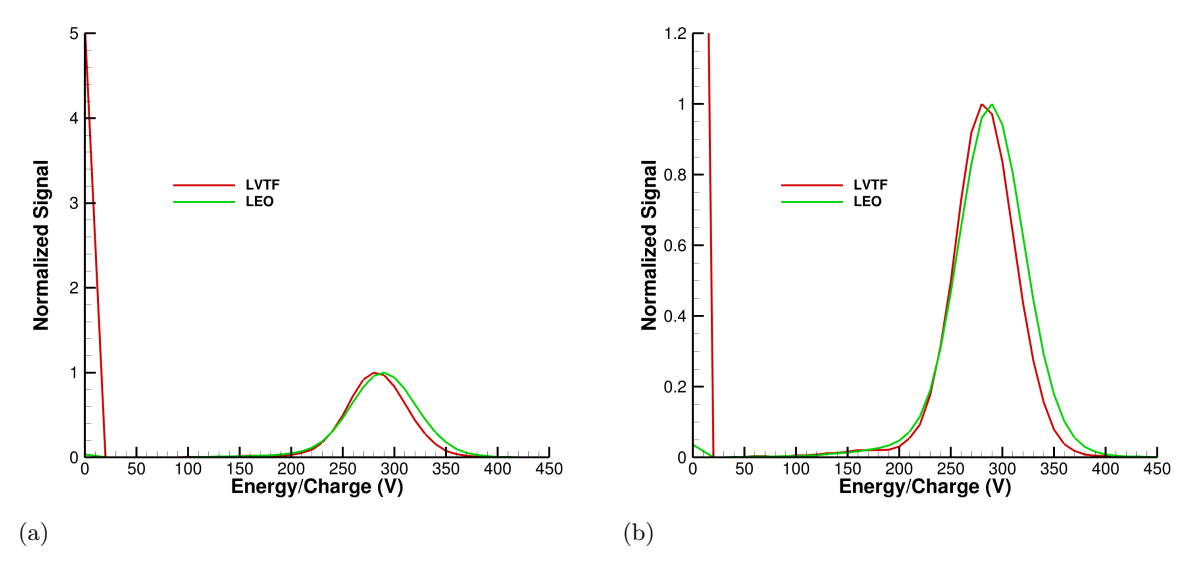


Figure 22: Centerline ion energy distributions 1.64 m downstream for LVTF and LEO simulations. Both panels present the same data with different y-axis limits: (a) the full-scale view highlights the pronounced low-energy spike, and (b) the zoomed view emphasizes the main-beam peak.

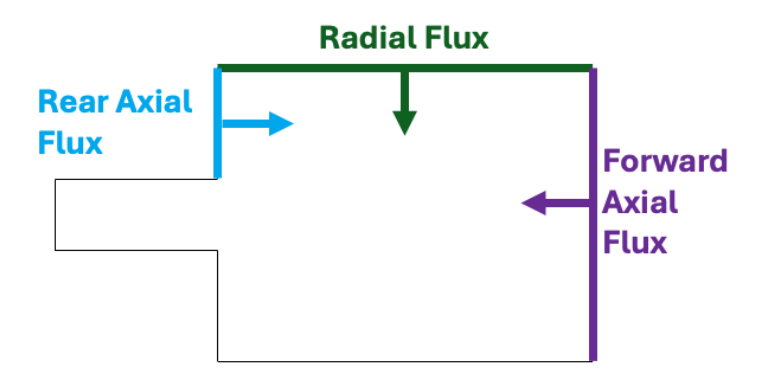


Figure 23: Diagram of thruster model boundaries over which the flux of neutrals moving from the plume model domain into the thruster model domain is calculated.

Table 5: Neutral flux into thruster near-field boundaries as calculated by plume simulations for different environments.

Environment	Forward Axial Flux $(particles m^{-2} s^{-1})$		Radial Flux $(particles m^{-2} s^{-1})$	Average Flux $(particles m^{-2} s^{-1})$
LVTF	8.0×10^{18}	8.7×10^{18}	7.6×10^{18}	8.1×10^{18}
LEO	1.6×10^{14}	1.4×10^{17}	1.5×10^{16}	5.1×10^{16}

IV. Conclusion

This work has presented coupled thruster-plume simulations of the H9 Hall-effect thruster in both a ground-based vacuum facility and a representative space environment. The comparisons highlight how



facility effects alter plasma behavior, underscoring the risks of extrapolating chamber data to flight conditions without accounting for these effects. Chamber simulations produced elevated neutral densities throughout the domain due to recirculation from physical walls and insufficient pumping capacity. Greater facility background pressure enhanced charge—exchange collisions and raised ion current density at large polar angles compared with space. From a spacecraft integration perspective, chamber data may substantially overpredict plume impingement on spacecraft surfaces. Electric potential contours also diverged between simulations of the two environments. Grounded chamber walls halted potential decay and suppressed ion acceleration in the far-field, shifting ion energy distributions measured along the centerline toward lower energies than in space. The neutral flux from the far-field into the near-field was quantified as a means of measuring the extent of the backpressure facility effect for a moderate-power HET in a large testing facility. The discrepancies are expected to grow as the community moves toward 100-kW class thrusters. The results emphasize the importance of explicitly modeling facility effects when interpreting or extrapolating measurements taken within non-ideal vacuum chambers. Predictive frameworks that couple high-fidelity thruster solvers with kinetic plume simulations, as demonstrated here, provide a path toward bridging the gap between ground tests and in-space operation.

Future work is planned to extend the modeling framework in several directions. Collisional processes for higher charge states are to be incorporated into the plume model, and charge-exchange products are to be included in the thruster model. Thruster physics may be enhanced by applying the particle-in-cell method to ions in place of the multi-fluid approach. The coupling scheme is expected to be improved by passing azimuthal velocities in addition to radial and axial velocities from the thruster to the plume solver. Passing detailed neutral flux values from the plume model back to the thruster model is planned to assess the potential impact of backpressure facility effects on thruster performance and lifetime. Spacecraft charging treatments will be expanded, and simulations will encompass a wider range of environments beyond LEO. The coupled system will be evaluated against experimental chamber data to strengthen confidence in extrapolations to space. Together these improvements are expected to enable more accurate predictions of thruster—plume behavior across a broad spectrum of mission scenarios and to support the design and qualification of high-power electric propulsion systems.

Appendix

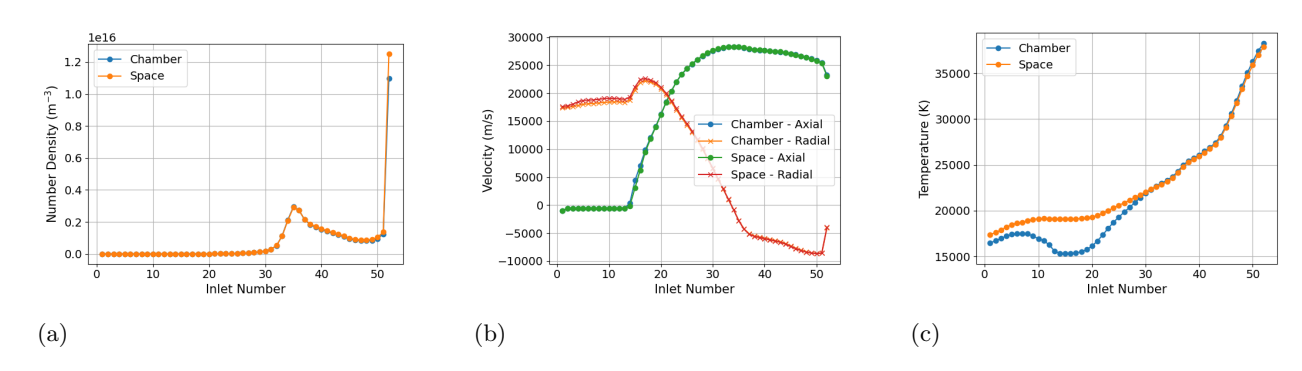


Figure 24: Profiles of Xe⁺⁺ population 1 properties across the thruster–plume interface: (a) number density, (b) velocity components, and (c) temperature, shown for both chamber and space simulations.

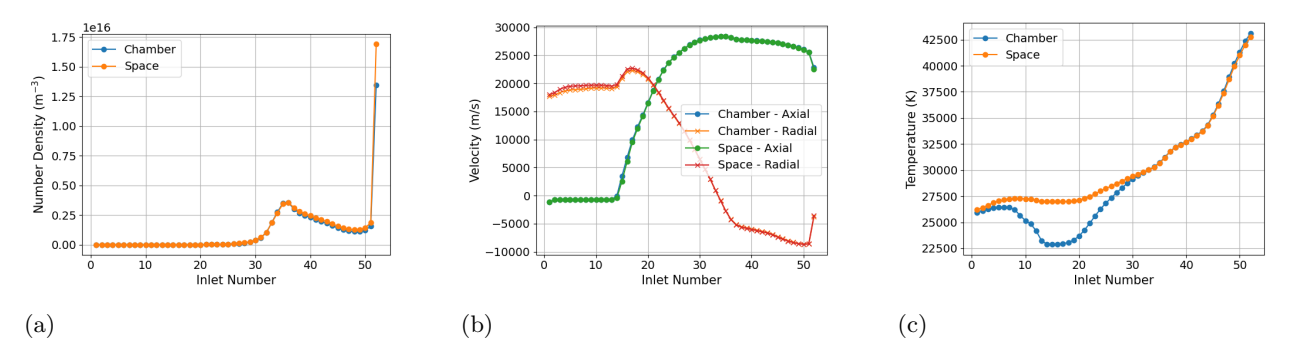


Figure 25: Profiles of Xe⁺⁺ population 2 properties across the thruster–plume interface: (a) number density, (b) velocity components, and (c) temperature, shown for both chamber and space simulations.

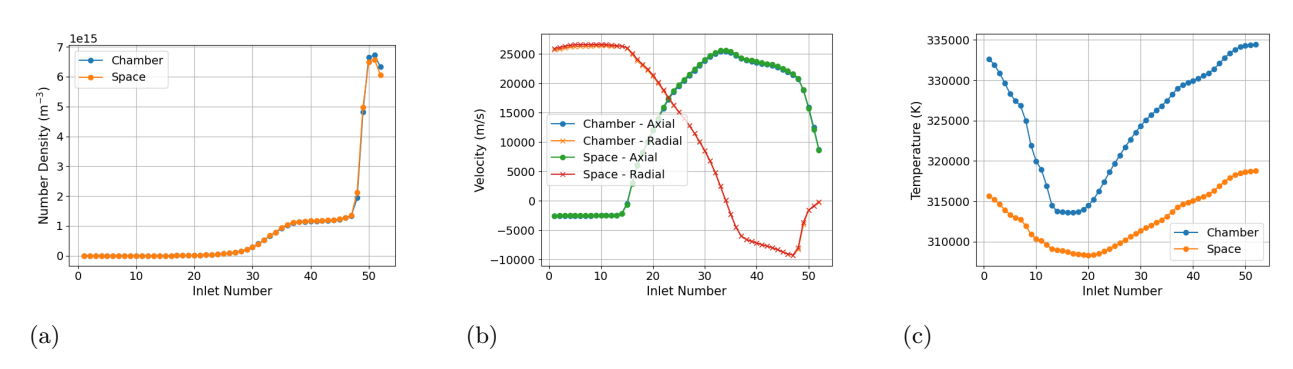


Figure 26: Profiles of Xe⁺⁺ population 3 properties across the thruster–plume interface: (a) number density, (b) velocity components, and (c) temperature, shown for both chamber and space simulations.

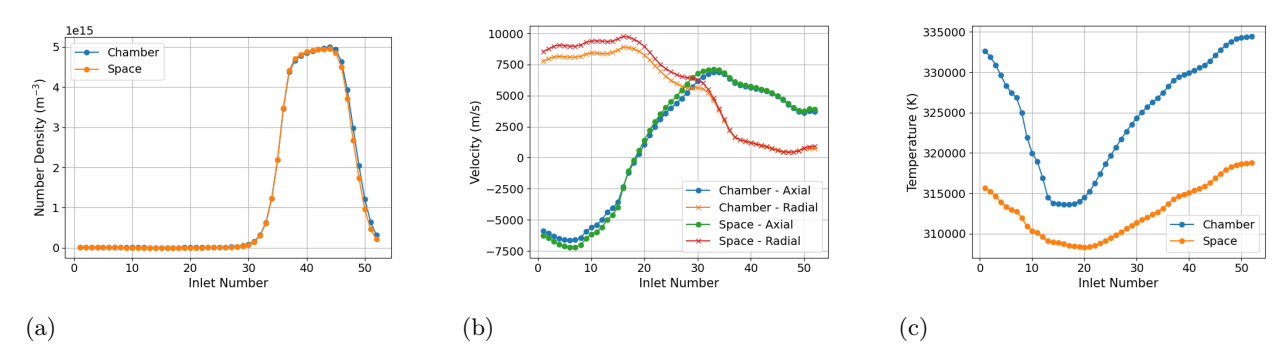


Figure 27: Profiles of Xe⁺⁺ population 4 properties across the thruster–plume interface: (a) number density, (b) velocity components, and (c) temperature, shown for both chamber and space simulations.

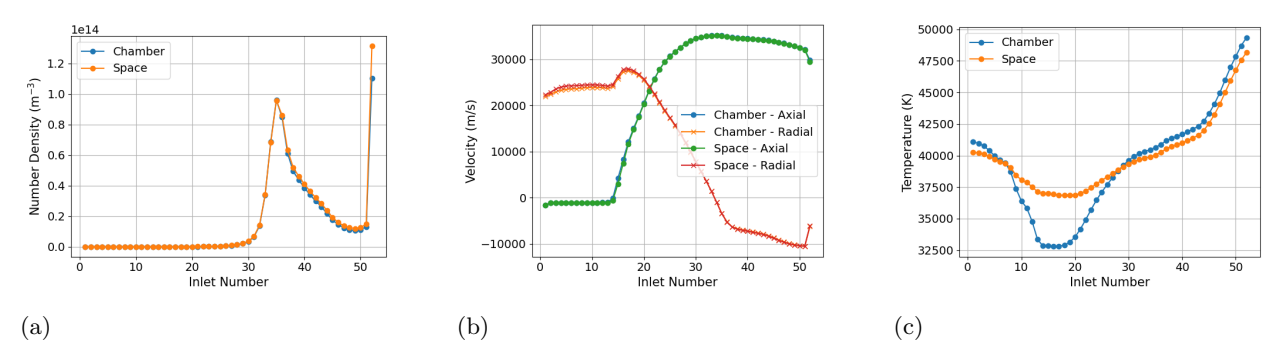


Figure 28: Profiles of Xe⁺⁺⁺ population 1 properties across the thruster–plume interface: (a) number density, (b) velocity components, and (c) temperature, shown for both chamber and space simulations.

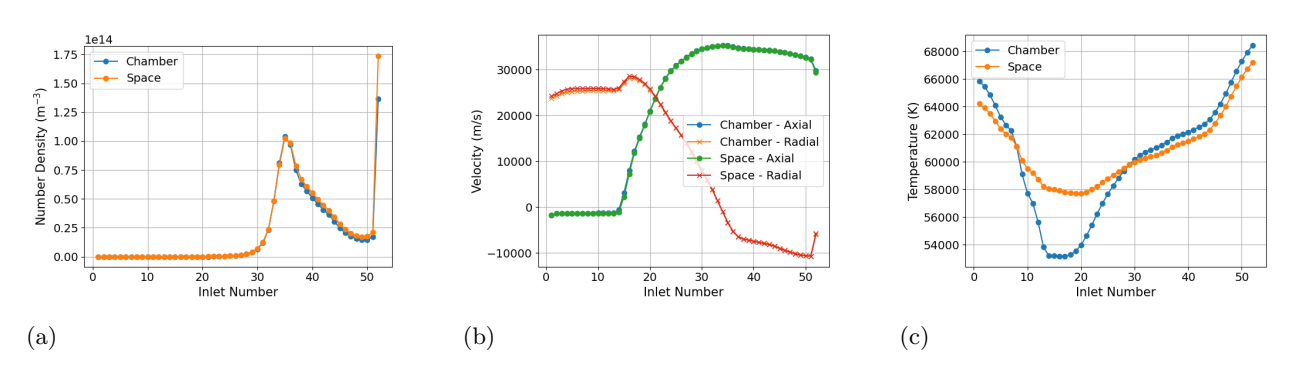


Figure 29: Profiles of Xe⁺⁺⁺ population 2 properties across the thruster–plume interface: (a) number density, (b) velocity components, and (c) temperature, shown for both chamber and space simulations.

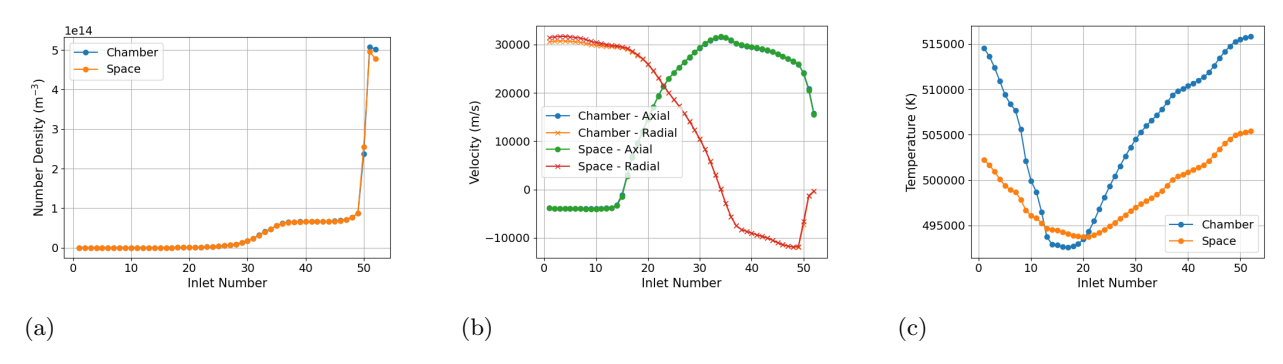


Figure 30: Profiles of Xe⁺⁺⁺ population 3 properties across the thruster–plume interface: (a) number density, (b) velocity components, and (c) temperature, shown for both chamber and space simulations.

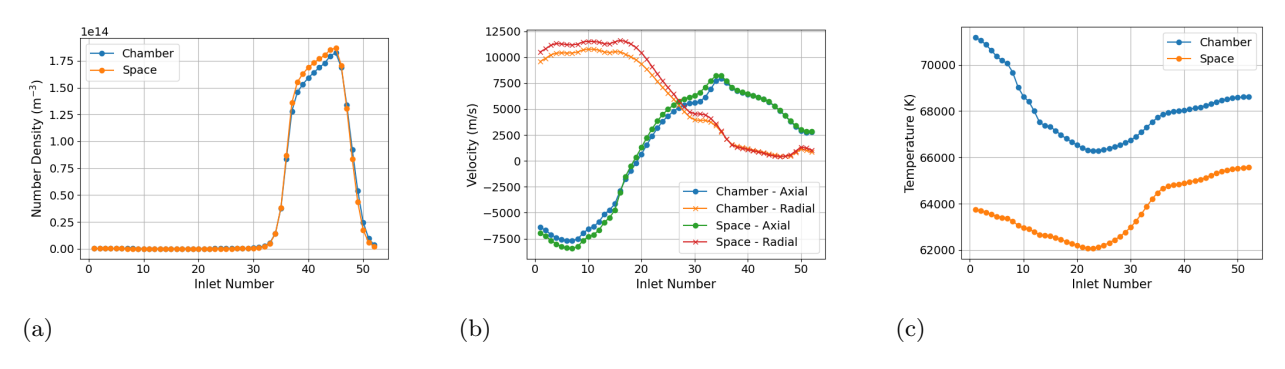


Figure 31: Profiles of Xe⁺⁺⁺ population 4 properties across the thruster–plume interface: (a) number density, (b) velocity components, and (c) temperature, shown for both chamber and space simulations.

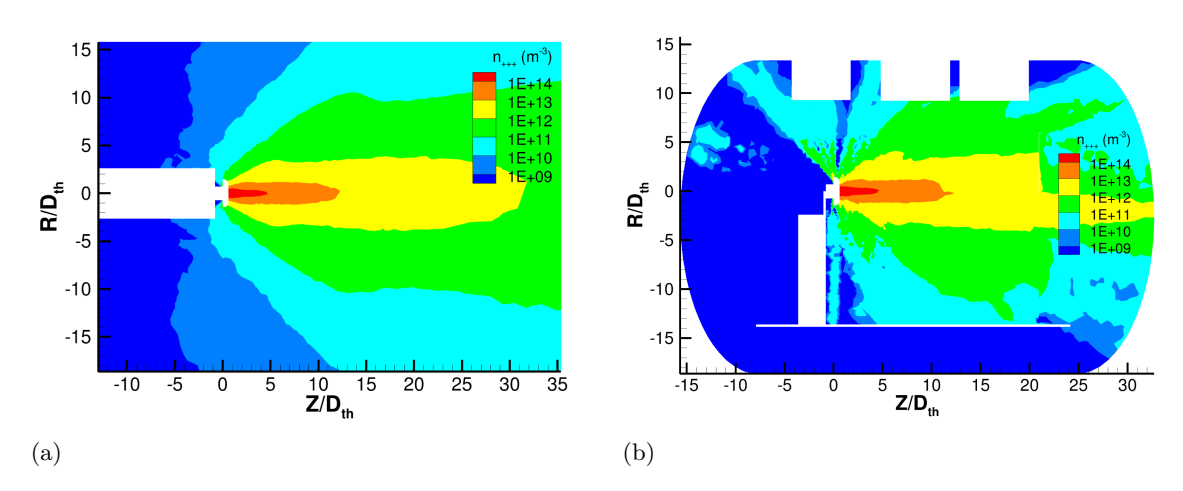


Figure 32: Triply charged ion number density contours: (a) simulation of the H9 HET in LEO and (b) simulation in the LVTF.

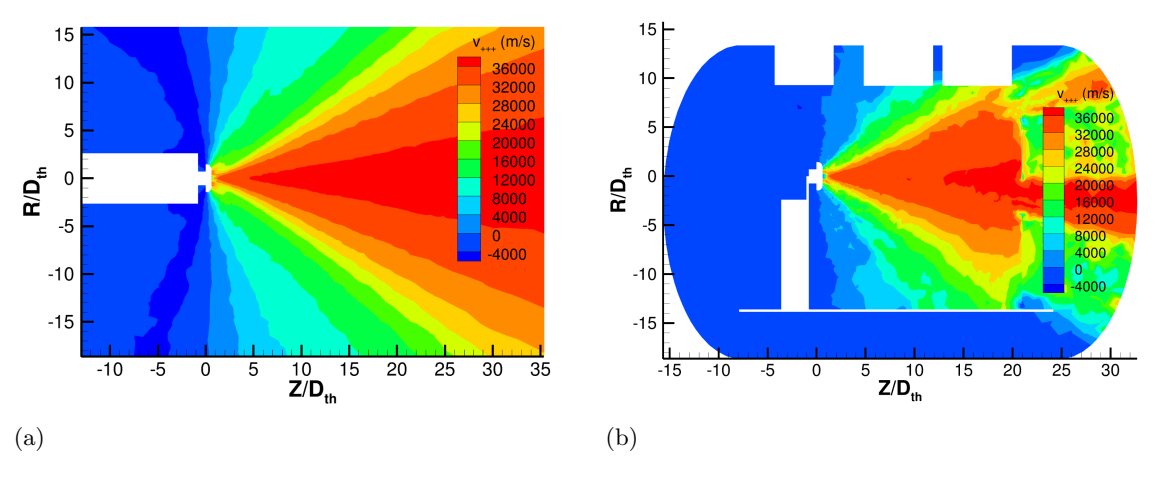


Figure 33: Triply charged ion axial velocity contours: (a) simulation of the H9 HET in LEO and (b) simulation in the LVTF.

Acknowledgments

This work was supported by NASA through the Joint Advanced Propulsion Institute, a NASA Space Technology Research Institute, grant number 80NSSC21K1118. This work utilized resources from the Univer-



sity of Colorado Boulder Research Computing Group, which is supported by the National Science Foundation, the University of Colorado Boulder, and Colorado State University. Resources supporting this work were also provided by the NASA High-End Computing Program through the NASA Advanced Supercomputing Division at Ames Research Center.

References

- ¹Saleh, J. H., Geng, F., Ku, M., and Walker II, M. L. R., "Electric Propulsion Reliability: Statistical Analysis of On-Orbit Anomalies and Comparative Analysis of Electric Versus Chemical Propulsion Failure Rates," *Space Weather*, Vol. 16, No. 10, 2018, pp. 1561–1569.
- ²Goebel, D. M. and Katz, I., Fundamentals of Electric Propulsion: Ion and Hall Thrusters, JPL Space Science and Technology Series, John Wiley and Sons, New Jersey, 2008.
- ³Mikellides, I. G., Ortega, A. L., Chaplin, V. H., and Snyder, J. S., "Facility pressure effects on a Hall thruster with an external cathode, II: Theoretical model of the thrust and the significance of azimuthal asymmetries in the cathode plasma," *Plasma Sources Science and Technology*, Vol. 29, No. 3, 2020.
- ⁴Cheng, S. Y. and Martinez-Sanchez, M., "Comparison of Numerical Simulation to Hall Thruster Plume Shield Experiment," 40th AIAA/ASME/SAE/ASEE Joint Propulsion Conference and Exhibit, No. AIAA 2004-3635, 2004.
- ⁵Huang, W., Kamhawi, H., Haag, T. W., Ortega, A. L., and Mikellides, I. G., "Facility Effect Characterization Test of NASA's HERMeS Hall Thruster," *AIAA Propulsion and Energy Forum*, 2016.
- ⁶Williams, G. J., Haag, T. W., Foster, J. E., Van Noord, J. L., and Malone, S. P., "Analysis of Pyrolytic Graphite Ion Optics Following the 2000-hr Wear Test of the HiPEP Ion Thruster," 42nd AIAA/ASME/SAE/ASEE Joint Propulsion Conference and Exhibit, No. AIAA-2006-5005, 2006.
- ⁷Walker, J. A., Langendorf, S. J., Walker II, M. L. R., Khayms, V., King, D., and Pertson, P., "Electrical Facility Effects on Hall Current Thrusters: Electron Termination Pathway Manipulation," *Journal of Propulsion and Power*, Vol. 32, No. 6, 2016, pp. 1365, 1377.
- ⁸Kamhawi, H., Huang, W., Haag, T., and Spektor, R., "Investigation of the Effects of Facility Background Pressure on the Performance and Voltage-Current Characteristics of the High Voltage Hall Accelerator," 50th AIAA/ASME/SAE/ASEE Joint Propulsion Conference and Exhibit, No. AIAA-2014-3707, 2014.
- ⁹Lipscomb, C. P., Boyd, I. D., Hansson, K. B., Eckels, J. D., and Gorodetsky, A. A., "Simulation of Vacuum Chamber Pressure Distribution with Surrogate Modeling and Uncertainty Quantification," AIAA Science and Technology Forum, 2024.
- 10 Mikellides, I. G. and Katz, I., "Numerical simulations of Hall-effect plasma accelerators on a magnetic-field-aligned mesh," *Physical Review E*, Vol. 86, 10 2012.
- ¹¹Lipscomb, C. P., Simulation of Hall Thruster Plasma Plume Expansion in Vacuum Chamber and Space Environments, Ph.D. thesis, University of Colorado Boulder, 2025, Ph.D. Dissertation, forthcoming.
- ¹²Ortega, A. L. and Mikellides, I. G., "The importance of the cathode plume and its interactions with the ion beam in numerical simulations of Hall thrusters," *Physics of Plasmas*, Vol. 23, No. 4, 04 2016, pp. 043515.
- ¹³Katz, I. and Mikellides, I. G., "Neutral gas free molecular flow algorithm including ionization and walls for use in plasma simulations," *Journal of Computational Physics*, Vol. 230, No. 4, 2011, pp. 1454–1464.
 - ¹⁴Bird, G. A., Molecular Gas Dynamics and the Direct Simulation of Gas Flows, Clarendon Press, 1994.
 - ¹⁵Birdsall, C. K. and Langdon, A. B., Plasma Physics Via Computer Simulation, Institute of Physics, 1991.
- ¹⁶Bird, G. A., "Monte-carlo simulation in an engineering context," Progress in Astronautics and Aeronautics, Vol. 74, 1981, pp. 239, 255.
- ¹⁷Boyd, I. D., "Review of Hall Thruster Plume Modeling," Journal of Spacecraft and Rockets, Vol. 38, No. 3, 2001, pp. 381, 387
- ¹⁸Boyd, I. D. and Dressler, R. A., "Far field modeling of the plasma plume of a Hall thruster," *Journal of Applied Physics*, Vol. 92, No. 4, 2002, pp. 1764, 1774.
- ¹⁹Miller, J. S., Pullins, S. H., Levandier, D. J., Chiu, Y., and Dressler, R. A., "Xenon charge exchange cross sections for electrostatic thruster models," *Journal of Applied Physics*, Vol. 91, No. 3, 2002, pp. 984, 991.
- ²⁰Katz, I., Jongeward, G., Davis, V., Mandell, M., Mikellides, I., Dressler, R., Boyd, I., Kannenberg, K., Pollard, J., and King, D., "A Hall Effect Thruster Plume Model Including Large-Angle Elastic Scattering," 37th AIAA/ASME/SAE/ASEE Joint Propulsion Conference and Exhibit, AIAA, Salt Lake City, UT, 2001.
 - ²¹Mitchner, M. and Kruger, C. H., *Partially Ionized Gases*, Wiley, New York, 1973.
- ²²Ahedo, E., Martinez-Cerezo, P., and Martinez-Sanchez, M., "One-dimensional model of the plasma flow in a Hall thruster," *Physics of Plasmas*, Vol. 8, No. 6, 2001, pp. 3058, 3068.
 - ²³Braginskii, S. I., "Transport Processes in a Plasma," Reviews of Plasma Physics, Vol. 1, 1965, pp. 205–311.
- ²⁴Viges, E. A., Jorns, B. A., Gallimore, A. D., and Sheehan, J. P., "University of Michigan's Upgraded Large Vacuum Test Facility," 36th International Electric Propulsion Conference, No. IEPC-2019-653, 2019.
- ²⁵Boyd, I. D., "Numerical Simulation of Hall Thruster Plasma Plumes in Space," *IEEE Transactions on Plasma Science*, Vol. 34, No. 5, 2006, pp. 2140, 2147.
- ²⁶Huismann, T. D. and Boyd, I. D., "Advanced Hybrid Modeling of Hall Thruster Plumes," 46th AIAA/ASME/SAE/ASEE Joint Propulsion Conference and Exhibit, No. AIAA 2010-6525, 2010.
- ²⁷Stephani, K. A. and Boyd, I. D., "Detailed modeling and analysis of spacecraft plume/ionosphere interactions in low Earth orbit," *Journal of Geophysical Research: Space Physics*, Vol. 119, No. 3, 2014, pp. 2101–2116.

